Carrier transport mechanisms in semiconductor nanostructures and devices

M. A. Rafiq[†]

Micro and Nano Devices Group, Department of Metallurgy and Materials Engineering, Pakistan Institute of Engineering and Applied Sciences, Islamabad, Pakistan

Abstract: Semiconductor nanostructures have gained importance due to their potential application in future nano-electronic devices. For such applications, it is extremely important to understand the electrical properties of semiconductor nanostructures. This review presents an overview of techniques to measure the electrical properties of individual and clusters of semiconductor nanostructures using microcopy based techniques or by fabricating metallic electrical contacts using lithography. Then it is shown that current–voltage (I–V) characteristics can be used to determine the conduction mechanism in these nanostructures. It has been explained that various material parameters can be extracted from I–V characteristics. The frequently observed conduction mechanism in these nanostructures such as thermally activated conduction, space charge limited current (SCLC), hopping conduction, Poole Frenkel conduction, Schottky emission and Fowler Nordheim (FN) tunneling are explained in detail.

Key words: semiconductor nanostructures; electrical conduction; electrical contacts; lithography; microscopy

1. Introduction

Semiconductor nanostructures are of great interest and importance to the research community due to their novel properties and interdisciplinary applications such as in nanoelectronics[1–8], nanophotonics[9–11], bio-sensing[12–16], optoelectronics[17–24], and solar cells[25–33]. Semiconductor nanostructures are also being considered as potential building blocks of post CMOS devices to sustain the scaling of devices[34]. Semiconductor nanostructures represent a unique system with one, two or three quantum confined directions for electron transport. Due to this semiconductor nanostructures have different electrical properties as compared to their bulk counterparts. High performance modern electronic devices can be designed by knowing the charge transport in semiconductor nanostructures and gaining control over it. Therefore, for utilization of semiconductor nanostructures in nanoelectronic devices it is extremely important to understand the electrical properties of these nanostructures. In order to probe the electrical properties of an individual nanostructure, electrical contacts must be made with the nanostructure. Owing to the small size of the nanostructure, this may not be an easy task. A rich variety of methods have already been developed and used for contacting individual nanostructures to explore their electron transport properties. Making an electrical contact to a cluster of nanostructures could be relatively easy. This review focuses on presenting an overview of such methods e.g. nano-fabricated electrodes, microscopy based methods and focused ion beam (FIB) techniques, and the current status of the research in this regard. This is followed by an overview of different types of transport mechanisms that are usually observed in nanostructures (e.g. thermally activated transport, space charge limited current, and hopping transport). In explaining these mechanisms, effort has been made to explain how various material parameters can be extracted from the measured I–V characteristics.

2. Making electrical contacts to semiconductor nanostructures

2.1. Fabrication of electrical contacts using lithography

Nanoelectronic devices utilizing single or multiple nanostructures can be fabricated using lithography in conjunction with standard microfabrication techniques. Fig. 1(a) shows a schematic diagram of a single nanowire device that can be used to measure the electrical properties of a semiconductor nanowire. The device is fabricated on an SiO_2 layer (~ 100 nm) grown thermally on the top-Si layer of SOI material. The top-Si layer is usually heavily doped and may be used as a back-gate. However, in this paper the effect of the gate on the electrical properties is not considered. Electrical contacts to multiple nanostructures such as nanowire forests and nanocrystal assemblies can be achieved using microfabrication techniques as well. As an example, Fig. 1(b) shows a scanning electron microscope (SEM) image of a nanowire device.

By using FIB induced metal deposition techniques, electrical contacts can be deposited to individual nanostructure[35–38]. An added advantage of the technique is that it can be used to sputter the oxide around the nanowire before deposition of contacts[39]. D'Ortenzi *et al.*[40] compared the FIB and lithography methods to form electrical contacts to silicon nanowires. They found that FIB is an efficient technique but lots of effort is required to avoid contamination. The lithography technique is a relatively cleaner method but the formation of a Schottky barrier at an electrical contact and nanowire interface cannot be avoided.

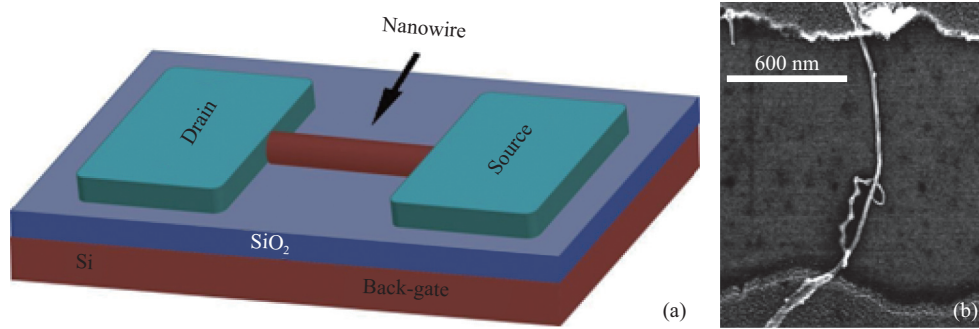Atomic force microscope (AFM) nanolithography[41, 42]

Fig. 1. (Color online) (a) Schematic diagram of a single nanowire device. (b) SEM image of a silicon nanowire contacted by microfabricated electrodes.
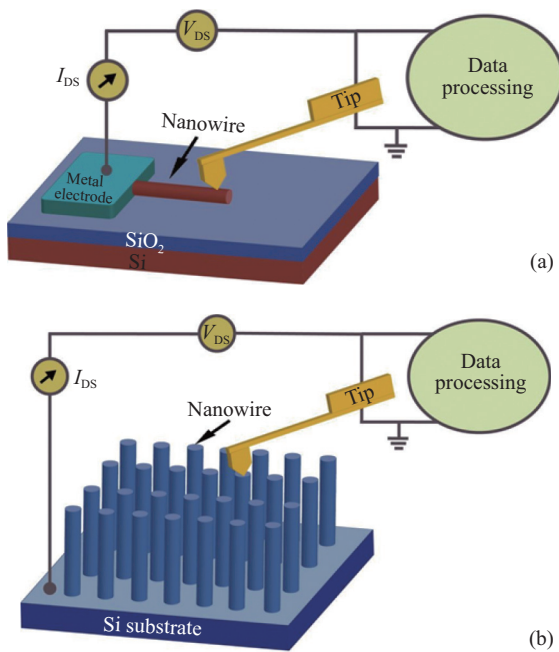

Fig. 2. (Color online) C-AFM experimental arrangements for electrical measurements of (a) a lateral nanowire and (b) a vertical nanowire.

is based on spatial confinement of chemical reactions and can be used to fabricate electrical contacts[43] to nanowires and thin films[44] as well as to fabricate nanodevices[41].

2.2. Microscopy based techniques to contact nanostructures

Conducting atomic force microscopy (C-AFM) utilizes conducting probes to measure I–V characteristics of nanostructures. This technique is also referred to as conducting probe atomic force microscopy (CP-AFM). The working principle of the technique is illustrated in Fig. 2 for electrical measurement of lateral and vertical nanowires. In Fig. 2(a) one side of the nanowire on SiO$_2$ is contacted with a micro-fabricated electrode and the conducting probe is positioned at desired points on the nanowire. A bias is applied to the conducting tip, and the resulting tip-sample current can be measured using external electronics. The added advantage here is that images of the nanowire can be taken before and after the electrical measurements using the AFM in tapping mode. Fig. 2(b) il-

lustrates that C-AFM can also be used to record I–V characteristics of vertical nanowires. More details about AFM as an electrical characterization tool for semiconductors in general can be found elsewhere[41].

C-AFM has been used to measure the resistivity of silicon nanowires grown by a chemical vapour deposition method using PtSi as catalyst[45], the electrical and photoconductive properties of individual ZnO nanowire[46], to confirm that SiO$_2$ coated CdTe nanowire had been properly insulated from the substrate, by comparing the I–V characteristics from coated and uncoated structures[47], to investigate the electrical properties of ZnO nanowires[48, 49], to measure the electrical and photoelectrical properties of the ZnO nanowire photodiode[50] and to study the electrical properties of nanoparticles and thin films[51, 52]. Using this technique, Zhou et al.[53, 54] measured the electron transport in InAs nanowire at different spacings between the fabricated electrode and the C-AFM tip. They demonstrated that for a tip-electrode spacing of less than 200 nm current flow was ballistic. For larger distances, the resistance increased linearly with distance as expected.

Erts et al.[55] used the arrangement shown in Fig. 2(b) to investigate the longitudinal conductivity of Ge nanowires in an anodic alumina template. Recently, Alvarez et al.[56] used C-AFM to study electrical properties of horizontal and vertical silicon nanowires.

SEM, transmission electron microscope (TEM) and scanning tunneling microscope (STM) has also been used to study electrical properties of nanostructures and nanodevices[57].

3. Transport mechanisms in semiconductor nanostructures

The most frequently observed transport mechanisms that were observed while analyzing I–V characteristics of semiconductor nanostructures are discussed in this section.

3.1. Space charge limited current (SCLC) transport

SCLC is a bulk limited transport mechanism and is often observed in materials with low free charge carrier concentration and ohmic contacts. In the SCLC transport mechanism[58, 59] if contacts are capable of injecting more charge into a material than the intrinsic charge, then the excess injected charge controls the current flow. Material features such as

trap distribution in the energy band gap, position of the Fermi energy and the charge carrier mobility can be obtained by applying the SCLC model.

3.1.1. Trap free SCLC

In case of trap free SCLC, the current density, J_{TF}, is given by[60],

$$J_{TF} = \frac{9\mu\varepsilon V^2}{8L^3}, \qquad (1)$$

where ε is the material's dielectric constant, L is the sample thickness (channel length), μ is the charge carrier mobility, and V is the applied voltage. However, Eq. (1) is valid for field independent μ and is also referred to as Child's law or the square law for trap free SCLC. However, it does not necessarily imply trap free material as Eq. (1) is also valid if the traps in the material have been filled.

For conductors with small diameter and high aspect ratio such as a semiconductor whiskers Eq. (1) is invalid[48]. Talin et al.[61, 62] developed a model to explain SCLC in nanowires with $R/L \ll 1$. Here R is the radius of the nanowire and L is the length of the nanowire. The model can be described by the equation:

$$J_{NW} = \zeta_0 \left(\frac{R}{L}\right)^{-2} \varepsilon\mu\frac{V^2}{L^3}. \qquad (2)$$

The constant ζ_0 is approximately unity. Initially at very low voltages ohmic behavior ($J_{ohmic} = ne\mu(V/L)$) is observed. The transition from ohmic to SCLC behavior occurs at a transition voltage V_t. At this voltage, the two current densities are equal i.e. $J_{NW} = J_{ohmic}$. Therefore, by determining V_t from the experimental I–V characteristics, carrier concentration can be determined. For nanowires:

$$n = \frac{\varepsilon V_t}{eR^2}. \qquad (3)$$

Talin et al.[61] investigated I–V characteristics of InAs nanowires using a nanoprobe. Fig. 3 shows the I–V curves of these nanowires as a log–log plot. The top left inset shows an image of the probe contacting one of the InAs NWs. The lower inset shows the I–V curves on the linear scale. An ohmic regain at lower voltages followed by the SCLC region can be clearly identified from the plot. By determining the transition voltage V_t from this plot, mobility and carrier concentration of InAS nanowires were calculated using Eqs. (2) and (3). Here the extracted carrier concentration range was $(0.5 \pm 0.3) \times 10^{17}$–$2.5 \times 10^{17}$ cm^{-3}, whereas the approximate mobility range was from 10–3500 cm^2/(V·s). The nanoprobe data shows that as the nanowire radius increases, mobility increases and n decreases. However, results obtained from FET geometry did not show such trends. The nanoprobe data as well as the trends are in reasonable agreement with recent transport measurements on InAs nanowires using the top-gate FET geometry reported by Dayeh et al.[63].

Using this SCLC model for nanowires Katzenmeyer et al.[64] showed that n and μ of InAs nanowires is diameter dependent. The nonlinear I–V characteristics of the GaN nanor-
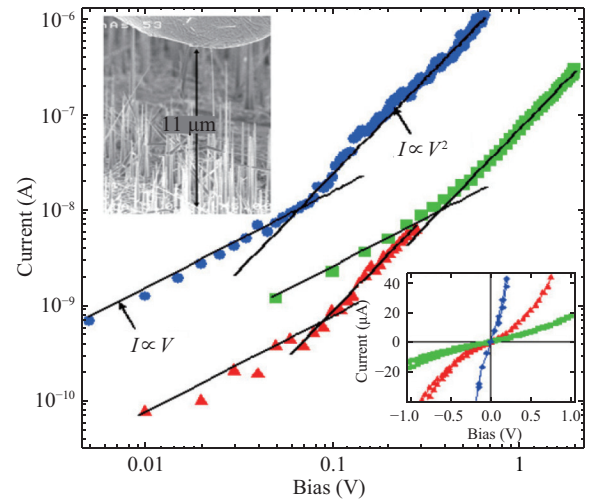

Fig. 3. (Color online) I–V curves for three InAs nanowires plotted on a log–log plot. Top inset shows an SEM image of a probe in contact with nanowire. The lower inset shows I–V curves on linear scale. From Ref. [61].

od have also been explained using the SCLC model for nanowires[62].

Using this model Zhao et al.[65] derived n to be ~10^{13}–10^{-15} cm^{-3} for InN nanowires depending on the radius of nanowires, and the range is in excellent agreement with the values of n obtained from the photoluminescence analysis[66]. They also calculated μ from the ohmic region of I–V curves, which was found to be 8000–12 000 cm^2/(V·s) for n~1 × 10^{13} cm^{-3} and is in reasonable agreement with theoretical calculations[67].

3.1.2. SCLC with traps

Traps are inevitable in materials prepared in the laboratory. Transport properties of nanowires are affected by traps such as surface traps that cause carrier depletion. The surface trap in nanowires can easily be incorporated during growth.

As long as greater charge is injected than the intrinsic charge, the magnitude and voltage dependence of the current are governed by the density and energy distribution of the traps. In case of exponential distribution of traps and holes, transport states are assumed to exist below an energy (above for electrons). The trap distribution exists above (below for electrons) these transport states. The presence of the trap distribution causes a reduction in free charge carriers and hence current. If a voltage is applied, the Fermi level moves (rises for electrons) towards the valance band in the energy gap (conduction band for electrons), thus filling any trap sites above (below for electrons) the Fermi level and making them unavailable to trap charge carriers. Therefore, as the injected charge increases, free carrier density increases rapidly resulting in a corresponding increase in the current[59].

To simplify the analysis of SCLC with an exponential distribution of traps it is assumed that only injected single carriers (holes or electrons) are considered, μ is field-independent and that the concentration of free charge carriers is much less than the concentration of trapped charge carriers.

For traps that are exponentially distributed within the en-

ergy band gap, the distribution function for the trap density can be written as[58, 68]:

$$h(E) = \frac{H_t}{E_t} \exp\left(\frac{-E}{E_t}\right),$$ (4)

where E is the relative energy measured from the bottom of conduction band. This trap distribution gives a power law dependence of the current density on the applied voltage and is given by:

$$J_{SCLC} = q^{1-l} \mu N_{DOS} \left(\frac{2l+1}{l+1}\right)^{l+1} \left(\frac{l}{l+1}\frac{\varepsilon}{H_t}\right)^l \frac{V^{l+1}}{L^{2l+1}}.$$ (5)

where H_t is the trap density, E_t is the characteristics constant of the distribution and is often written in terms of characteristic trap temperature T_t ($E_t = k_B T_t$, k_B is the Boltzmann constant), N_{DOS} is the density of states (DOS) in the relevant band, $l = T_t/T$, here T is the measurement temperature. Eq. (5) clearly shows the power law dependence of the form J–V^m with $m = l + 1$.

Since $l = T_t/T$, $m = l + 1$ can be written as $m = (T_t/T) + 1$. As $T_t = E_t/k_B$, m can be expressed as:

$$m = \left(\frac{E_t}{k_B T}\right) + 1.$$ (6)

The parameter m is the slope of the $\log J_{SCLC}$–$\log V$ plot at all measurement temperatures. From Eq. (6) it is clear that, once m is known for all measurement temperatures, characteristic energy E_t can be determined from the slope of a plot of m versus $1/T$.

An Arrhenius form of the Eq. (5) is given below[69]:

$$J_{SCLC} = \left(\frac{\mu_p N_v q V}{L}\right) f(l) \exp\left[-\frac{E_t}{kT} \ln\left(\frac{qH_t L^2}{2\varepsilon V}\right)\right],$$ (7)

where

$$f(l) = \left(\frac{2l+1}{l+1}\right)^{l+1} \left(\frac{l}{l+1}\right)^l \frac{1}{2^l}.$$ (8)

For $l > 2$, $f(l) \sim 0.5$, Eq. (7) therefore becomes:

$$J_{SCLC} = \frac{1}{2}\left(\frac{\mu_p N_v q V}{L}\right) \exp\left[-\frac{E_t}{kT} \ln\left(\frac{qH_t L^2}{2\varepsilon V}\right)\right].$$ (9)

This clearly gives activation energy:

$$E_a = \frac{E_t}{k} \ln\left(\frac{qH_t L^2}{2\varepsilon V}\right),$$ (10)

where E_a is the slope of $\log J_{SCLC}$ versus $1/T$ curves at certain voltage. E_t can be obtained from Eq. (6). Parameters L, V, ε and q are known for a particular experiment. Therefore, the trap density H_t can be estimated by determining the slope of the $\log J_{SCLC}$ versus $1/T$ curve at a constant voltage.

Eq. (9) shows that at crossover voltage (where $E_a = 0$) the current is approximately temperature independent therefore Eq. (10) implies:
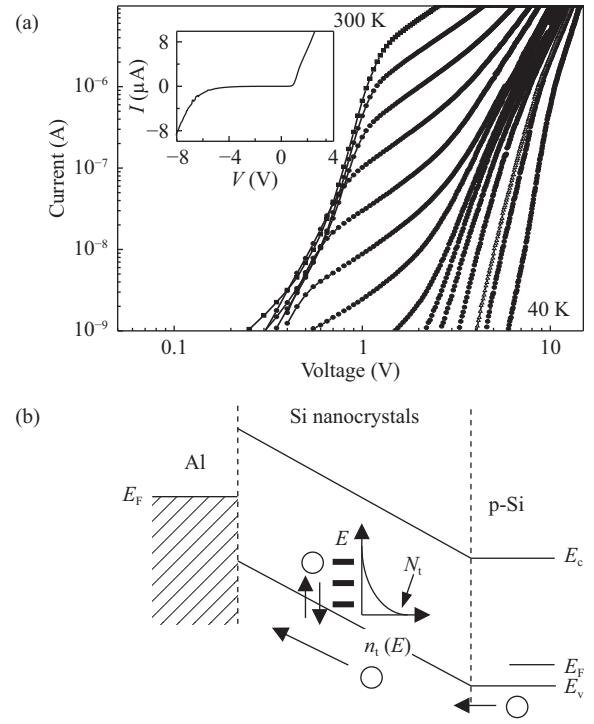

Fig. 4. I–V characteristics of a $35 \times 35 \mu m^2$ diode from 300 to 40 K, on a log–log plot. The temperature step is 20 K. The inset shows the I–V characteristics at 300 K, from −8 to 4 V, on a linear scale. (b) Schematic diagram of SCLC transport. The SiO_2 potential barriers in the Si nanocrystal film are omitted for clarity. Carriers (holes) are injected from the p-Si substrate into the film. An exponential distribution of traps $n_t(E)$ exists in the film. From Ref. [70].

$$V_c = \frac{qH_t L^2}{2\varepsilon}.$$ (11)

Here sample thickness L, the electronic charge q and the dielectric constants ε are known for the given material. V_c can be obtained by plotting temperature dependent J_{SCLC}–V curves on the log–log plot for two or three temperatures and extrapolating the power law. The trap density H_t then can be determined from Eq. (11). This is a much simpler approach as compared to other approaches for the determination of the trap density[70]. The J_{SCLC}–V characteristics that can be fitted by the power law J_{SCLC}–V^m with $m > 2$, are attributed to SCLC with an exponential distribution of traps[58, 71].

Rafiq et al. reported SCLC with an exponential distribution of traps in 300 nm thick films of size-controlled silicon nanocrystals[70]. The electrical measurements were performed on Al/Si nanocrystal/p-Si/Al structure. Fig. 4(a) shows I–V characteristics of these Si nanocrystal films from 40 to 300 K on the log–log graph with 40 K temperature step. From the graph, it is clear that from 300 to 200 K the I–V curves tend to meet at the cross over voltage. A schematic diagram of the SCLC mechanism with exponential distribution of traps is shown in Fig. 4(b). Fig. 5 shows the power law fits from 300 to 200 K to find the value of the slope m. The inset shows that as temperature decreases m increases. From this curve, characteristic trap temperature T_t and characteristic trap energy $E_t = k_B T$ can be found. A cross over voltage 17 V was determined from the main graph. Using this cross over voltage, a trap density of 2.4×10^{17} cm^{-3} in the Si nano-
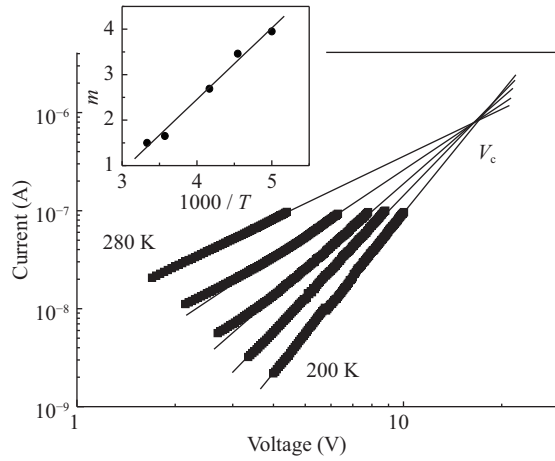
Fig. 5. Power law fits to the data of Fig. 4 from 280 to 200 K, with a temperature step of 20 K. The fits meet at cross over voltage $V_c = 17$ V. The inset shows m as a function of inverse temperature. From Ref. [70].

crystal film was determined using Eq. (11). Rasool *et al.* used the same technique to find out the trap density in vertical silicon nanowire arrays[72].

Xu *et al.*[73] observed SCLC with an exponential distribution of traps in GaSb nanowires. They determined that characteristics trap energy reduces from 0.26 to 0.12 eV after annealing indicating that annealing reduces the deep trap level in the nanowires. They attributed oxygen impurity as a possible trap source in GaSb nanowires.

Schricker *et al.*[74] investigated temperature dependant *I–V* characteristics of GaAs nanowires. They observed $J_{SCLC}–V^m$ dependence with $m > 2$ indicating the presence of SCLC with an exponential distribution of traps. By using the procedure outlined earlier they obtained characteristic trap energies ranging from 0.024 to 0.11 eV below the band edge. The trap density range was from 1×10^3 to 1.2×10^{15} cm^{-3}. From the analysis of *I–V* curves they concluded that the Fermi level shifts towards the band edge indicating the presence of impurities or the surface state in the nanowires.

SCLCs with traps have been reported in InN nano wires[65] and Si nanowires[56] as well. Liao *et al.*[75] studied the adsorbates effect on the SCLC in a ZnO nanowire. In this case free carriers are strongly depleted by surface adsorbates and the electron transport properties are dominated by the injected carriers and desorption of oxygen in air and vacuum eliminated SCLC.

From *I–V* characteristic measurements in vacuum, dry N_2, and ambient air it was found that CdS nanowires became more resistive in air[76]. This is attributed to oxygen adsorption from air that depletes the nanowires. These oxygen depleted nanowires exhibited SCLC with an exponential distribution of traps with $m > 2$. From the m versus $1/T$ plot, the characteristic trap energy was estimated to be 0.18–0.37 eV with an average value of 0.28 ± 0.04 eV.

3.2. Thermally activated transport
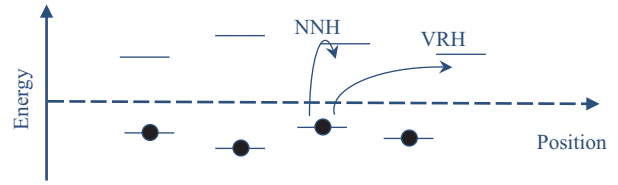
For thermally activated transport the conductivity is given by:

Fig. 6. Schematic diagram to illustrate the concept of NNH and VRH.

$$\sigma = \sigma_0 \exp(-E_a/k_B T), \tag{12}$$

where σ_0 is a temperature-independent prefactor and E_a corresponds to the thermal activation energy. This type of conduction is usually observed at higher temperatures. For example in the case of FeS$_2$ nanorods[77] thermally activated transport is observed from 300–400 K. However as will be explained later, at lower temperatures hopping transport is observed in these nanorods. Such transport has been observed in single CdS nanowire[76]. Activation energy can be obtained by determining the slope of lnσ versus $1/T$ plot.

3.3. Hopping conduction

In the hopping conduction mechanism, electrons 'hop' from one localized state to another localized state by phonon assisted tunnelling. Hopping conduction is of two types, nearest neighbour hopping (NNH) and variable range hopping (VRH) as shown schematically in Fig. 6. In case of NNH, the electron hop to the nearest neighbor sites and temperature dependence of conductivity is of activation type. However, in case of VRH, an electron does not necessarily hop to a nearest neighbour. Rather, the electron tries to hop to a site that requires the least activation energy for the process.

The VRH concept was proposed by Mott[78, 79] and is called Mott's VRH. A generalized form of Mott's VRH in *d*-dimensions is:

$$\sigma = \sigma_0 \exp\left(-\frac{T_M}{T}\right)^{\frac{1}{d+1}}, \tag{13}$$

where σ_0 is a constant of proportionality and depends weakly on temperature. The values of σ_0 can be found in Ref. [80] and TM is given by:

$$T_M = \frac{18}{\alpha^3 N(E_F) k_B}, \tag{14}$$

where α is the localization length and $N(E_F)$ is the DOS at the Fermi energy E_F. If lnσ versus $(1/T)^{1/(d+1)}$ is plotted then the slope of this graph yields the value of T_M. Then using Eq. (14) $N(E_F)$ can be obtained if the localization length is known. For 3D Mott VRH, the most probable hopping distance and average hopping energy are given by[81]:

$$R_{hop,Mott} = \frac{3}{8}\alpha\left(\frac{T_M}{T}\right)^{1/4}, \tag{15}$$

and

$$W_{hop,Mott} = \frac{1}{4}k_B T\left(\frac{T_M}{T}\right)^{1/4}. \tag{16}$$

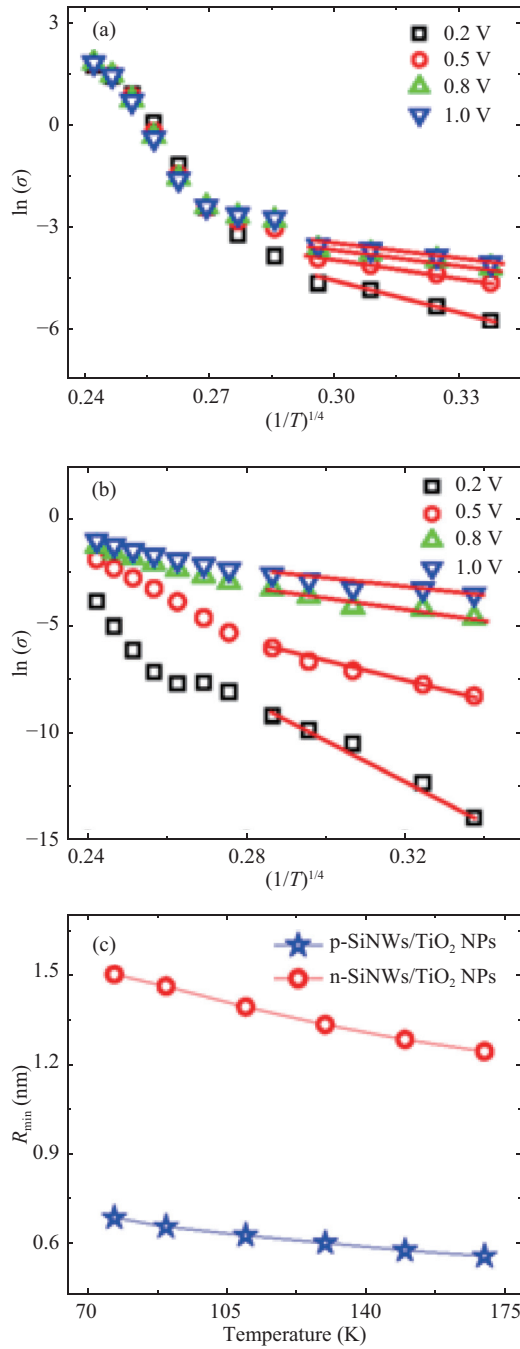Figs. 7(a) and 7(b) show the lnσ versus $(1/T)^{1/4}$ plots for

Fig. 7. (Color online) lnσ versus $(1/T)^{1/4}$ plot for (a) p-Si nanowires/TiO$_2$ nanoparticles and (b) n-Si nanowires/TiO$_2$ nanoparticles hybrid device. The data clearly obey the 3D Mott variable range hopping mechanism from 170 to 77 K as indicated by the solid line. (c) Minimum hopping distance R_{min} versus temperature plot for both devices. Here SiNWs stands for silicon nanowires and NPs stands for nanoparticles. From Ref. [72].

vertical p-Si nanowires/TiO$_2$ nanoparticles and vertical n-Si nanowires/TiO$_2$ nanoparticles hybrid devices, respectively[72]. In both devices, the 3D Mott VRH is the dominant conduction mechanism from 170 to 77 K. By determining the value T_M from Figs. 7(a) and 7(b), the values of $N(E_F)$ were found to be 8.39 × 10^{21} and 1.05 × 10^{21} eV^{-1} cm^3 for p-Si nanowires/TiO$_2$ nanoparticles and n-Si nanowires/TiO$_2$ nanoparticle hybrid devices at 0.5 V, respectively. Fig. 7(c) shows the variation of hopping distance with temperature for both

devices. Paschoal et al.[82] found $N(E_F) = 4.0 \times 10^{18}$ (eV·cm^3)$^{-1}$ in Mn ion-implanted GaAs nanowire. Imran et al.[83] reported 3D Mott VRH in perovskite CdTiO$_3$ nanofibers and calculated the density of states, minimum hopping distance and hopping energy for the nanofibers using the Mott VRH model. Recently Jian et al.[84] has reported 2D Mott VRH in ZnO nanoflakes. From the 2D Mott VRH data they estimated a localization length of ~7 nm, consistent with the radius of ZnO nanoflake grain determined using TEM.

Efros and Shkovskii[80] suggested that in the presence of Coulomb interactions, the value of the exponent in Eq. (13) is 1/2. They argued that in the presence of Coulomb interactions the DOS for any localized state vanishes at the Fermi level. This Coulomb gap originates due to the electron-hole pairs generated as an electron hops from a site, leaving a hole behind. In this case, the DOS is proportional to $(E-E_F)^2$. Further, in this case, the activation energy is inversely proportional to the hopping distance. Therefore, the conductivity in this case can be written as[80]:

$$\sigma \propto \exp\left[-\left(\frac{T_{ES}}{T}\right)^{1/2}\right], \quad (17)$$

where

$$T_{ES} = \frac{2.8e^2}{\kappa \alpha k_B}, \quad (18)$$

where κ is the static dielectric constant. Eq. (17) is usually referred to as the Efros-Shkovskii (ES) law for hopping conduction.

Above a crossover temperature T_c the Coulomb interactions can be neglected and conductivity obeys Motts VRH law[81, 85] and below T_c the ES law is valid. The T_c is given by:

$$T_c = 16\frac{T_{ES}^2}{T_M}. \quad (19)$$

Below T_c the most probable hopping distance and hopping energy are given by[81]:

$$R_{hop,ES} = \frac{1}{4}\alpha\left(\frac{T_{ES}}{T}\right)^{1/2}, \quad (20)$$

and

$$W_{hop,ES} = \frac{1}{2}k_B T\left(\frac{T_{ES}}{T}\right)^{1/2}. \quad (21)$$

Haung et al.[81] studied VRH in oxygen deficient polycrystalline ZnO films. They found that in these films the cross over from ES to Mott VRH occurs at a few tens of degree kelvin. From the experimental data, they found the DOS, hopping distance and hopping energy for both ES and Mott VRH cases. Mukherjee et al.[86] observed a crossover from 3D Mott VRH to ES VRH at ~12 K in Sb doped ZnO thin film. The experimentally observed crossover temperature was close to the theoretically calculated crossover temperature (~16 K) using Eq. (19). Li et al.[87] observed a transition from
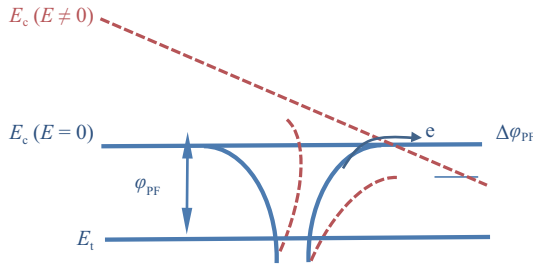
Fig. 8. (Color online) Schematic diagram of the Poole Frenkel effect. The φ_{PF}, E_c and E_t represent the Poole Frenkel barrier height, conduction band energy and trap energy respectively.

ES to Mott VRH at 25 K in polycrystalline germanium thin films.

At temperatures greater T_A, Arrhenius behaviour is observed[85]. The T_A is given by

$$T_A = \left(\frac{\alpha}{4d_1}\right)^2 T_{ES}, \tag{22}$$

where d_1 is the nearest neighbour distance.

Temperature dependent I–V characteristics of FeS_2 nanorods using four-probe geometry, from 40–220 K have shown the presence of Mott VRH in these nanorods. However, a thermally activated transport from 300–400 K has been observed with an activation energy 100 meV[77]. Similarly Mott VRH has been observed in GaAs nanowire[88]. Temperature dependant I–V curves of ZnO nanowires prepared by CVD have shown that ES VRH is dominant in ZnO nanowires from 300–6 K[89].

Pichon et al.[90] investigated the temperature dependence of the electrical properties of doped polycrystalline Si nanowires from 200–530 K. The conductivity in these nanowires obeys 3D Mott VRH. From the VRH model they determined the corresponding DOS following exponential distributions linked to the statistical shift of the Fermi level.

3.4. Poole Frenkel conduction

The Poole Frenkel conduction is a bulk limited conduction mechanism. In Poole Frenkel conduction, the trapped charge carriers by impurities in the band gap of a semiconductor can be transferred to the conduction by the applied field. In the case of Poole Frenkel conduction, impurity is regarded as an ionized donor with a hydrogen-like Coulomb potential. For Poole Frenkel conduction, the trap center should be neutral when filled by a charge carrier. On application of an external field potential well distorts (Poole Frenkel barrier reduces by an amount $\Delta\varphi_{PF} = \beta_{PF}E^{1/2}$) and charge carrier can easily overcome the barrier to go to the conduction band of the semiconductor as shown schematically in Fig. 8.

The Poole Frenkel current density is given by[91]:

$$J_{PF} = \sigma_0 E \exp\left[\beta_{PF}E^{1/2}/k_B T\right]. \tag{23}$$

Here σ_0 is low field conductivity and E is average electric field. The Poole Frenkel field lowering coefficient β_{PF} is given by:
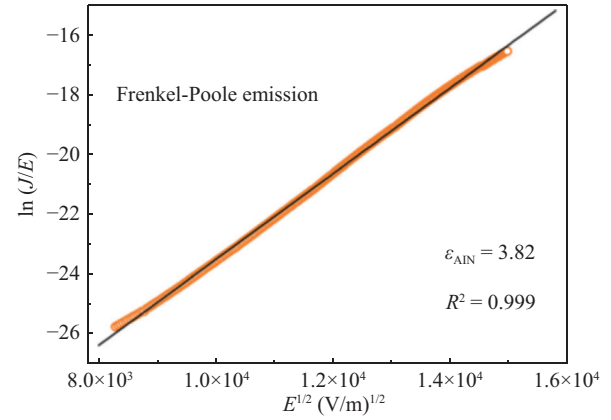

Fig. 9. (Color online) Poole Frenkel plot of AlN thin film. From Ref. [92].

$$\beta_{PF} = \left(\frac{q^3}{\pi\varepsilon_r\varepsilon_0}\right)^{1/2}, \tag{24}$$

where ε_r is the relative dielectric constant, ε_0 is permittivity of free space and q is electronic charge. From Eq. (1) it can be seen that in the case of Poole Frenkel conduction a plot of $\ln J_{PF}$ against $E^{1/2}$ should show a linear relationship. From the slope of this plot, the field lowering coefficient can be determined. Once the field lowering coefficient is known, the dielectric constant of the material can be determined from Eq. (24).

Fig. 9 shows the Poole Frenkel curve for atomic layer deposited AlN thin film at applied field in the range 63.8–211.8 MV/m[92]. From the slope of this curve the calculated value of the dielectric constant of the AlN films is 3.8. This value of the dielectric constant of AlN film agrees with the optical and static dielectric constants.

Jeong et al.[93] extracted a value of 2.8 for the dielectric constant of atomic-layer-deposited HfO_2 films from the slope of the Poole Frenkel plots. It is known that the optical dielectric constant is equal to the square of the refractive index. The refractive index of HfO_2 is 1.7–1.9. Therefore, the extracted value of the dielectric constant of HfO_2 films is close to the square of the refractive index. This indicates that Poole Frenkel plots can be used to determine the dielectric constant of materials. Similarly, Son et al.[94] determined appropriately the dielectric constant values of nitrided Hf-silicate gate dielectric. Chiu et al.[95] determined a value of refractive index 1.7 ± 0.1 for Pr_2O_3 MIS capacitors from Poole Frenkel plots, and it was close to the value obtained by the optical method.

Poole Frenkel data can also be used to calculate trap energies, which helps us to understand the various aspects of traps in a semiconductor. For example, Yeh et al.[96] determined Pool Frenkel trap energies in thin films of Al_2O_3 and Hf_xAl_yO with different Al and Hf compositions. It is concluded that the trap energy increases with Al content in the Hf_xAl_yO thin film.

The Poole Frenkel conduction mechanism has also been observed in vertical silicon nanowires[97], individual SiC nanowires[98], porous silicon layers[99], ZnO thin films[100], Barium Managanate nanorods[101] and GaAs nanowires[102].
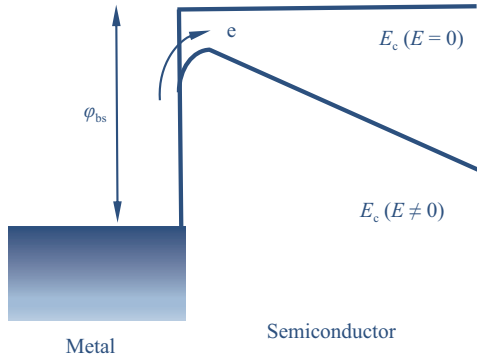
Fig. 10. (Color online) Schematic diagram of Schottky emission.

3.5. Schottky emission

Schottky emission is a contact limited process. In this process the barrier formed at the metal semiconductor interface is lowered due to the applied electric field as shown schematically in Fig. 10. According to the thermionic emission model the forward current voltage characteristics of a Schottky contact neglecting the series resistance can be expressed as[103]:

$$I = I_s \left[\exp\left(\frac{qV}{nk_BT} \right) - 1 \right], \tag{25}$$

whereas

$$I_s = AA^* T^2 \exp\left(-\frac{q\varphi_{bs}}{k_BT} \right), \tag{26}$$

where A is the diode area, I_s is the saturation current, n is the ideality factor, A^* is Richardson constant (120 A/cm^2/K^2) and φ_{bs} is the Schottky barrier height of the diode. The forward bias current including the diode series resistance (R_s) is given by:

$$I = I_s \exp\left[\frac{q(V - IR_s)}{nk_BT} \right]. \tag{27}$$

Chenung *et al.* suggested that Eq. (27) can be written as:

$$\frac{dV}{d(\ln I)} = \frac{nk_BT}{q} + IR_s. \tag{28}$$

Therefore, slope and intercept of the plot of dV/d(ln$I$) and I will yield series resistance and ideality factor of the diode respectively. To evaluate the barrier height a new function $H(I)$ is defined as follows:

$$H(I) = \eta\varphi_b + IR_s. \tag{29}$$

As the ideality factor is already known, the intercept of the plot between $H(I)$ and I will give the barrier height of the diode. Therefore, if I–V characteristics of a metal semiconductor diode are measured, it is possible to find out all three parameters of the fabricated diode. The method was used in Ref. [104] to determine the ideality factor, series resistance and barrier height of Pt/ZnO thin film Schottky diodes. It was found that barrier height, ideality factor and series resistance were 0.71 eV, 2.5 and ~95 Ω, respectively. Using the same ap-

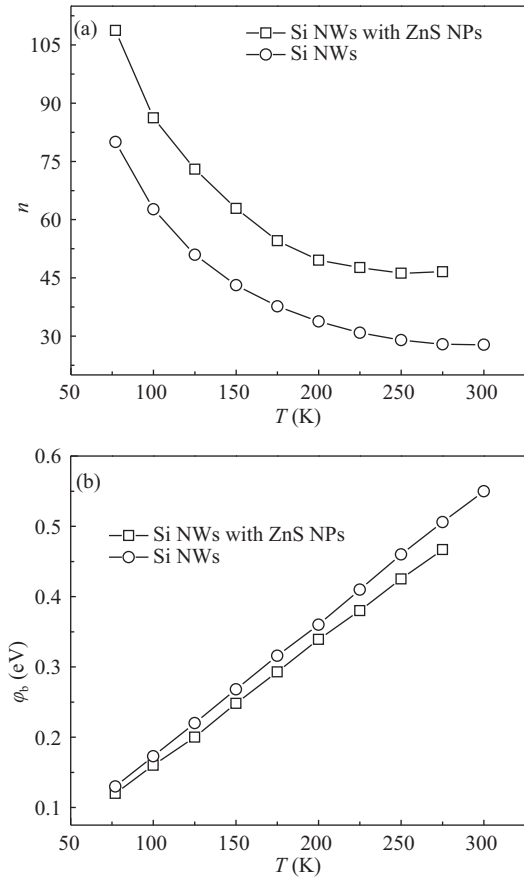Fig. 11. Temperature dependence of a) ideality factor (n) and b) barrier height φ_b calculated from fitting of the Schottky emission equation of p$^+$-Si nanowires decorated with and without ZnS nanoparticles. Here NWs stand for nanowires and NPs stand for nanoparticles. From Ref. [106].

proach Quereda *et al.*[105] studied the effect of local strain on all three Schottky diode parameters of atomic force microscope/MoS$_2$ flakes/ITO substrate back to back Schottky diodes. It was found that the resistance of MoS$_2$ flake decreases with an increase in applied load, and the saturation current of the tip-MoS$_2$ barrier increases, indicating a pressure-induced lowering of the barrier potential. However, they found no effect on the ideality factor and saturation current of the flake-substrate diode.

Furthermore Ahmad *et al.*[106] determined ideality factor and barrier heights for the Au/vertical p$^+$-SiNWs coated with ZnS nanoparticle diodes. Figs. 11(a) and 11(b) show the ideality factors and barrier heights calculated for this diode. A huge deviation of ideality factor in this diode was attributed to the large mismatch of lattice[107]. Moreover, the non-ideal values of the barrier height and ideality factor are attributed to interface specific effects[108–111].

3.6. FN tunneling

The FN conduction is a contact limited process. It is quantum mechanical phenomena and is the dominant conduction mechanism through thin insulting layers and thin films. Such insulting layers are part of the metal oxide semiconductor (MOS) structures that frequently occur in integrated struc-
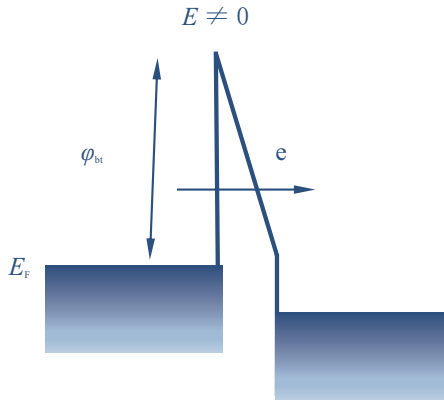
Fig. 12. (Color online) Schematic diagram of tunnelling through metal insulator metal structure.

tures. Fig. 12 shows the FN tunneling process schematically. The FN tunneling current density through an oxide layer is given by[103, 112, 113]:

$$J_{FN} = A_1 E^2 \exp\left(-\frac{B_1}{E}\right), \qquad (30)$$

where

$$A_1 = \frac{m}{m^*}\frac{q^3}{8\pi h\varphi_{bt}}, \qquad (31)$$

$$B_1 = \frac{8\pi}{3}\left(2\frac{m^*}{h^2}\right)^{1/2}\frac{\varphi_{bt}{}^{3/2}}{q}. \qquad (32)$$

Here E, m, m^*, h, and φ_{bt} are applied field, electron mass, electron effective mass in silicon dioxide, Plank's constant and the tunneling barrier height at the injecting electrode, respectively. According to this model a plot between $\log(J_{FN}/E^2)$ and $1/E$ is a straight line with B_1 as the slope. Therefore, by constructing a graph between $\log(J_{FN}/E^2)$ and $1/E$ the tunneling barrier height can be found. FN tunneling has been used to determine the FN tunneling parameters of MOS structures[112, 114].

FN tunneling governs the field emission phenomena from semiconductor nanostructures. Field emission is a form of quantum tunneling in which electrons are emitted from a material held at negative biased towards an anode through a vacuum barrier by a strong electric field. Field emission has vast technological applications in various disciplines such as displays and electron microscopy. The field emission current is given by[115]:

$$J_{FE} = \left(A_2\frac{\beta^2 E^2}{\varphi}\right)\exp\left(-B_2\frac{\varphi^{3/2}}{\beta E}\right), \qquad (33)$$

$$I = S J_{FE}, \quad E = \frac{V}{d_2}, \qquad (34)$$

$$\ln\left(\frac{J_{FE}}{E^2}\right) = \ln\left(A_2\frac{\beta^2}{\varphi}\right) - B_2\frac{\varphi^{3/2}}{\beta E}, \qquad (35)$$

where $A_2 = 1.54\times10^{-6}$ A·eV·V^{-2} and $B_2 = 6.83\times10^3$ eV$^{-3/2}$ V/μm. S is the area of the emitter, V is applied voltage, I is emission current, β is the field enhancement factor, d_2 is the distance
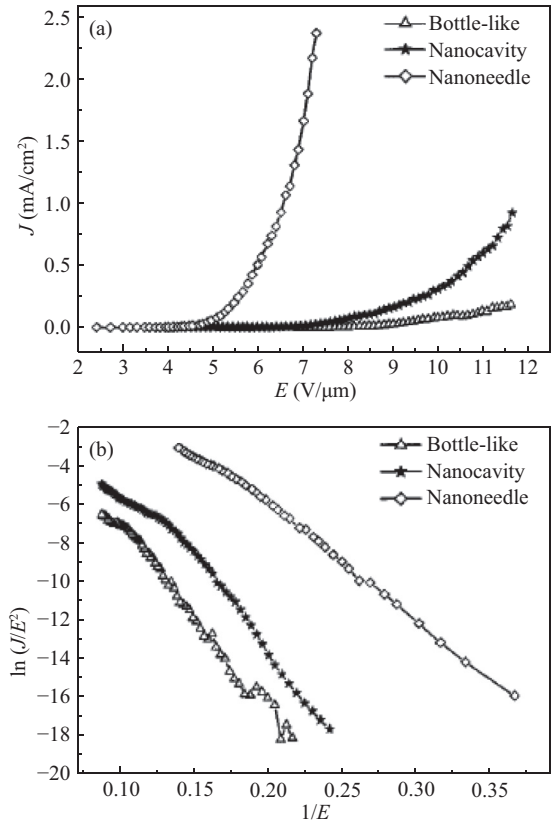

Fig. 13. (a) J_{FE}–E plots of field emission from ZnO nanorod arrays and (b) corresponding FN plots. From Ref. [116].

between the tip of the emitter and the anode, and j is the work function of the emitter. The field-enhancement factor ($\beta = h/r$, h is height and r is radius of emitter) is related to emitter geometry. Therefore, longer emitters with sharp tips greatly increase emission current.

Zhao et al.[116] studied the field emission from ZnO nanorod arrays with different morphologies. Figs. 13(a) and 13(b) show $J_{FE}E$ plots and the corresponding FN plot at a working distance of 460 μm for ZnO nanorod arrays respectively. Nanoneedle arrays showed the best field emission properties (Fig. 13(a)). They determined field enhancement factor β from the slope of the FN plot (Fig. 13 (b)), which is a straight line confirming the FN tunnelling. From the data, they found out that the nanoneedle array had the lowest turn on the field, highest β and largest emission efficiency due to the smallest radius.

She et al.[117] studied the correlation between resistance and field emission properties of single one dimensional ZnO nanostructures. They found that field emission from low resistance ZnO emitters is better. Moreover, the high resistance region in ZnO nanostructure causes a vacuum breakdown event. They concluded that the uniform conductivity of nanostructures is important for field emission applications.

Sun et al.[118] showed that field emission properties of graphene were improved by decorating it with ZnO quantum dots. The field emission from semiconductor nanostructures has been the subject of a large number studies[119–129].

3.7. Band to band tunnelling

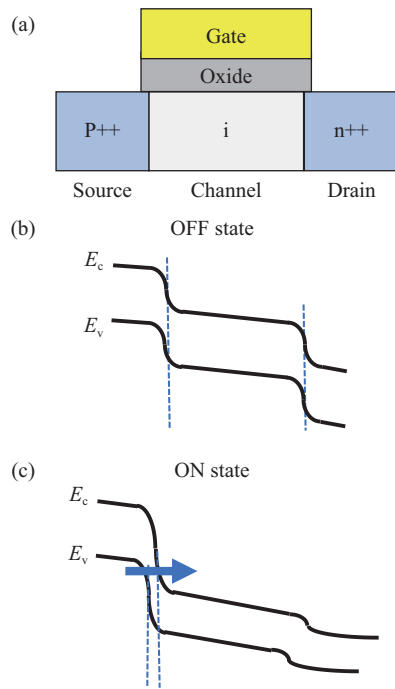Band-to-band tunneling was first discovered by Zener in

Fig. 14. (Color online) (a) Schematic diagram of n-type TFET. (b) Band diagram of the TFET in OFF state and (c) band diagram of the TFET in ON state.

1934[130]. It is a phenomenon in which an electron tunnels from the valence band to the conduction band of a semiconductor through the band gap without the assistance of traps. This phenomenon is being utilized in tunneling field effect transistors (TFETs)[131, 132]. The TFETs are being considered leading contenders to outperform CMOS at low voltages[133, 134]. This is due to the fact that a subthreshold swing of less than 60 mV per decade can be attained in these devices at room temperature. A lower subthreshold swing reduces the supply voltage and enables a path to lower system power. Fig. 14(a) shows schematically an n-type TFET consisting of reverse biased p–i–n structure. The source is grounded in this case and positive voltages are applied to source and drain. Fig. 14(b) shows the corresponding band diagram of the TFET in OFF state. With zero gate voltage the tunneling distance indicated by the vertical dashed lines is large. When positive voltage is applied to the gate, bands in the channel move down and the tunneling distance shrinks as shown by the vertical dashed lines in Fig. 14(c). This allows band to band tunneling and the device is in ON state now. TFET has been studied extensively in the literature using different semiconductor materials and different device structures[135–145]. More recently 2D materials such as graphene[146], black phosphorous[147] and transition metal dichalcogenides[148] have been used to fabricate TFETs. Roy *et al.*[149] reported a subthreshold swing of approximately 100 mV per decade at room temperature and ON/OFF ratio of 10^7 in the WSe$_2$ and SnSe$_2$ heterostructures. The interlayer band to band tunneling has been demonstrated in vertical MoS$_2$/WSe$_2$ heterostructures[150, 151]. One dimensional materials such as carbon nanotubes have been used to study the TFET[152, 153]. For further details about band to band tunnelling and TFETs the reader is referred to the cited references in this section and the references therein.

4. Concluding remarks

Different methods to make electrical contacts to single and clusters of nanostructures to explore the electrical properties are presented. The most popular method, however, is to fabricate electrical contacts to the nanostructures using a standard nano/micro fabrication process. However, C-AFM, nanoprobe with SEM and four-tip STM are also being used to measure electrical properties. A great deal of information can be obtained from the I–V characteristics of nanostructures. The temperature dependant I–V curves can be used to find the prevailing transport mechanism in the nanostructures. Various material parameters e.g. trap density, dielectric constant, number of charge carriers, mobility and density of localized states can be determined by carefully analysing the I–V curves.

References

[1] Chau R, Doyle B, Datta S, et al. Integrated nanoelectronics for the future. Nat Mater, 2007, 6: 810

[2] Cui Y. Functional nanoscale electronic devices assembled using silicon nanowire building blocks. Science, 2001, 291: 851

[3] Akinwande D, Petrone N, Hone J. Two-dimensional flexible nanoelectronics. Nat Commun, 2014, 5: 5678

[4] Burghard M, Klauk H, Kern K. Carbon-based field-effect transistors for nanoelectronics. Adv Mater, 2009, 21: 2586

[5] Bubnova O. Nanoelectronics: a 2D microprocessor. Nat Nanotechnol, 2017, 8: 14948

[6] Lieber C M, Wang Z L. Functional nanowires. MRS Bull, 2007, 32: 99

[7] Rafiq M A, Durrani Z A K, Mizuta H, et al. Room temperature single electron charging in single silicon nanochains. J Appl Phys, 2008, 103: 053705

[8] Oda S, Huang S Y, Salem M A, et al. Charge storage and electron/light emission properties of silicon nanocrystals. Phys E, 2007, 38: 59

[9] Xia F, Wang H, Xiao D, et al. Two-dimensional material nanophotonics. Nat Photonics, 2014, 8: 899

[10] Bimberg D. Quantum dot based nanophotonics and nanoelectronics. Electron Lett, 2008, 44: 390

[11] Gonsalves F C, Klein K, Carson B B, et al. An RNAi-based chemical genetic screen identifies three small-molecule inhibitors of the Wnt/wingless signaling pathway. Proc Natl Acad Sci, 2011, 108: 5954

[12] Rahman M M, Ahammad A J S, Jin J H, et al. A comprehensive review of glucose biosensors based on nanostructured metal–oxides. Sensors, 2010, 10: 4855

[13] Gallay P, Tosi E, Madrid R, et al. Glucose biosensor based on functionalized ZnO nanowire/graphite films dispersed on a Pt electrode. Nanotechnology, 2016, 27: 425501

[14] Betty C A. Nanostructured semiconductor based biochemical sensors. Mater Sci Technol, 2016, 32: 375

[15] Tereshchenko A, Bechelany M, Viter R, et al. Optical biosensors based on ZnO nanostructures: Advantages and perspectives. A review. Sens Actuators B, 2016, 229: 664

[16] Frasco M F, Chaniotakis N. Semiconductor quantum dots in chemical sensors and biosensors. Sensors, 2009, 9: 7266

[17] Priolo F, Gregorkiewicz T, Galli M, et al. Silicon nanostructures for photonics and photovoltaics. Nat Nanotechnol, 2014, 9: 19

[18] Li H, Wang X, Xu J, et al. One-dimensional CdS nanostructures: a promising candidate for optoelectronics. Adv Mater,

2013, 25: 3017

[19] Jie J, Zhang W, Bello I, et al. One-dimensional II–VI nanostructures: synthesis, properties and optoelectronic applications. Nano Today, 2010, 5: 313

[20] Bisi O, Ossicini S, Pavesi L. Porous silicon: a quantum sponge structure for silicon based optoelectronics. Surf Sci Rep, 2000, 38: 1

[21] Djurii A B, Ng A M C, Chen X Y. ZnO nanostructures for optoelectronics: material properties and device applications. Prog Quantum Electron, 2010, 34: 191

[22] Rasool K, Rafiq M A, Ahmad M, et al. Photodetection and transport properties of surface capped silicon nanowires arrays with polyacrylic acid. AIP Adv, 2013, 3: 082111

[23] Ahmad M, Rasool K, Rafiq M A, et al. Enhanced and persistent photoconductivity in vertical silicon nanowires and ZnS nanoparticles hybrid devices. Appl Phys Lett, 2012, 101: 223103

[24] Rasool K, Rafiq M A, Ahmad M, et al. TiO_2 nanoparticles and silicon nanowires hybrid device: role of interface on electrical, dielectric, and photodetection properties. Appl Phys Lett, 2012, 101: 253104

[25] Zhang Q, Dandeneau C S, Zhou X et al. ZnO nanostructures for dye-sensitized solar cells. Adv Mater, 2009, 21: 4087

[26] Rath A K, Bernechea M, Martinez L et al. Solution-processed heterojunction solar cells based on p-type PbS quantum dots and n-type Bi_2S_3 nanocrystals. Adv Mater, 2011, 23: 3712

[27] Nozik A. Quantum dot solar cells. Phys E, 2002, 14: 115

[28] Kamat P V. Quantum dot solar cells: semiconductor nanocrystals as light harvesters. J Phys Chem C, 2008, 112: 18737

[29] Ali N, Hussain A, Ahmed R, et al. Advances in nanostructured thin film materials for solar cell applications. Renew Sustain Energy Rev, 2016, 59: 726

[30] Zhang G, Finefrock S, Liang D, et al. Semiconductor nanostructure-based photovoltaic solar cells. Nanoscale, 2011, 3: 2430

[31] Yu M, Long Y Z, Sun B, et al. Recent advances in solar cells based on one-dimensional nanostructure arrays. Nanoscale, 2012, 4: 2783

[32] Sivakov V, Andrä G, Gawlik A, et al. Silicon nanowire-based solar cells on glass: synthesis, optical properties, and cell parameters. Nano Lett, 2009, 9: 1549

[33] Stelzner T, Pietsch M, Andrä G, et al. Silicon nanowire-based solar cells. Nanotechnology, 2008, 19: 295203

[34] Hayden O, Agarwal R, Lu W. Semiconductor nanowire devices. Nano Today, 2008, 3: 12

[35] Chen C Y, Chang P H, Tsai K T et al. Electrical and optoelectronic characterization of a ZnO nanowire contacted by focused-ion-beam-deposited Pt. INEC 2010 3rd International Nanoelectronics Conference, 2010, 20: 1177

[36] Motayed A, Davydov A V, Vaudin M D, et al. Fabrication of GaN-based nanoscale device structures utilizing focused ion beam induced Pt deposition. J Appl Phys, 2006, 100: 24306

[37] Hernández-Ramírez F, Tarancón A, Casals O, et al. Fabrication and electrical characterization of circuits based on individual tin oxide nanowires. Nanotechnology, 2006, 17: 5577

[38] Vilà A, Hernández-Ramirez F, Rodríguez J, et al. Fabrication of metallic contacts to nanometre-sized materials using a focused ion beam (FIB). Mater Sci Eng C, 2006, 26: 1063

[39] Cronin S B, Lin Y M, Rabin O, et al. Making electrical contacts to nanowires with a thick oxide coating. Nanotechnology, 2002, 13: 653

[40] D'Ortenzi L, Monsù R, Cara E, et al. Electrical contacts on silicon nanowires produced by metal-assisted etching: a comparative approach. Nanoscale Res Lett, 2016, 11: 468

[41] Notargiacomo A, Foglietti V, Cianci E, et al. Atomic force microscopy lithography as a nanodevice development technique. Nanotechnology, 1999, 10: 317

[42] Xie X N, Chung H J, Sow C H, et al. Nanoscale materials patterning and engineering by atomic force microscopy nanolithography. Mater Sci Eng R, 2006, 54: 1

[43] Calleja M, Garcıa R. Nano-oxidation of silicon surfaces by noncontact atomic-force microscopy: size dependence on voltage and pulse duration. Appl Phys Lett, 2000, 76: 3427

[44] Bark H, Kwon S, Lee C. Bias-assisted atomic force microscope nanolithography on NbS_2 thin films grown by chemical vapor deposition. J Phys D, 2016, 49: 484001

[45] Baron T, Gordon M, Dhalluin F, et al. Si nanowire growth and characterization using a microelectronics-compatible catalyst: PtSi. Appl Phys Lett, 2006, 89: 233111

[46] Fan Z, Dutta D, Chien C J, et al. Electrical and photoconductive properties of vertical ZnO nanowires in high density arrays. Appl Phys Lett, 2006, 89: 213110

[47] Liang X, Tan S, Tang Z et al. Investigation of transversal conductance in semiconductor CdTe nanowires with and without a coaxial silica shell. Langmuir, 2004, 20: 1016

[48] Sakurai M, Wang Y G, Uemura T, et al. Electrical properties of individual ZnO nanowires. Nanotechnology, 2009, 20: 155203

[49] He J H, Ho C H. The study of electrical characteristics of heterojunction based on ZnO nanowires using ultrahigh-vacuum conducting atomic force microscopy. Appl Phys Lett, 2007, 91: 233105

[50] He J H, Ho S Te, Wu T B, et al. Electrical and photoelectrical performances of nano-photodiode based on ZnO nanowires. Chem Phys Lett, 2007, 435: 119

[51] Wu F, Cai W, Gao J, et al. Nanoscale electrical properties of epitaxial Cu_3Ge film. Sci Rep, 2016, 6: 28818

[52] Guo E, Zeng Z, Shi X, et al. Electrical transport properties of au nanoparticles and thin films on Ge probed using a conducting atomic force microscope. Langmuir, 2016, 32: 10589

[53] Dayeh S A. Electron transport in indium arsenide nanowires. Semicond Sci Technol, 2010, 25: 24004

[54] Zhou X, Dayeh S A, Aplin D, et al. Direct observation of ballistic and drift carrier transport regimes in InAs nanowires. Appl Phys Lett, 2006, 89: 053113

[55] Erts D, Polyakov B, Daly B, et al. High density germanium nanowire assemblies: contact challenges and electrical characterization. J Phys Chem B, 2006, 110: 820

[56] Alvarez J, Ngo I, Gueunier-Farret M E, et al. Conductive-probe atomic force microscopy characterization of silicon nanowire. Nanoscale Res Lett, 2011, 6: 110

[57] Zhang Q, Li H, Gan L, et al. In situ fabrication and investigation of nanostructures and nanodevices with a microscope. Chem Soc Rev, 2016, 45: 2694

[58] Kao K C, Hwang W. Electrical transport in solids: with particular reference to organic semiconductors. Pergamon Press, 1981

[59] Lampert M A, Mark P. Current injection in solids. Science, 1970, 170: 966

[60] Mott N F, Gurney R W. Electronic processes in ionic crystals. New York: Dover Publications, 1964

[61] Talin A A, Léonard F, Katzenmeyer A M, et al. Transport characterization in nanowires using an electrical nanoprobe. Semicond Sci Technol, 2010, 25: 24015

[62] Talin A A, Léonard F, Swartzentruber B S, et al. Unusually strong space-charge-limited current in thin wires. Phys Rev Lett, 2008, 101: 76802

[63] Dayeh S A, Yu E T, Wang D. Transport coefficients of InAs nanowires as a function of diameter. Small, 2009, 5: 77

[64] Katzenmeyer A M, Léonard F, Talin A A, et al. Observation of space-charge-limited transport in InAs nanowires. IEEE

Trans Nanotechnol, 2010, 10: 92

[65] Zhao S, Salehzadeh O, Alagha S, et al. Probing the electrical transport properties of intrinsic InN nanowires. Appl Phys Lett, 2013, 102: 073102

[66] Zhao S, Fathololoumi S, Bevan K H, et al. Tuning the surface charge properties of epitaxial InN nanowires. Nano Lett, 2012, 12: 2877

[67] Stoica T, Meijers R J, Calarco R, et al. Photoluminescence and intrinsic properties of MBE-grown InN nanowires. Nano Lett, 2006, 6: 1541

[68] Chiguvare Z, Dyakonov V. Trap-limited hole mobility in semiconducting poly(3-hexylthiophene). Phys Rev B, 2004, 70: 1

[69] Matsumoto T, Mimura H, Koshida N, et al. Deep-level energy states in nanostructural porous silicon. Jpn J Appl Phys, Part 1, 1999, 38: 539

[70] Rafiq M A, Tsuchiya Y, Mizuta H, et al. Charge injection and trapping in silicon nanocrystals. Appl Phys Lett, 2005, 87: 1

[71] Mark P, Helfrich W. Space-charge-limited currents in organic crystals. J Appl Phys, 1962, 33: 205

[72] Rasool K, Rafiq M A, Ahmad M, et al. Charge injection and trapping in TiO_2 nanoparticles decorated silicon nanowires arrays. Appl Phys Lett, 2015, 106: 073101

[73] Xu W, Chin A, Ye L, et al. Charge transport and trap characterization in individual GaSb nanowires. J Appl Phys, 2012, 111: 104515

[74] Schricker A D, Davidson F M, Wiacek R J et al. Space charge limited currents and trap concentrations in GaAs nanowires. Nanotechnology, 2006, 17: 2681

[75] Liao Z M, Lv Z K, Zhou Y B, et al. The effect of adsorbates on the space–charge-limited current in single ZnO nanowires. Nanotechnology, 2008, 19: 335204

[76] Gu Y, Lauhon L J. Space-charge-limited current in nanowires depleted by oxygen adsorption. Appl Phys Lett, 2006, 89: 143102

[77] Cabán-Acevedo M, Liang D, Chew K S, et al. Synthesis, characterization, and variable range hopping transport of pyrite (FeS2) nanorods, nanobelts, and nanoplates. ACS Nano, 2013, 7: 1731

[78] Mott N F. Conduction in glasses containing transition metal ions. J Non Cryst Solids, 1968, 1: 1

[79] Mott N F. Conduction and switching in non-crystalline materials. Philos Mag, 1969, 19: 835

[80] Shklovskii B I, Efros A L. Electronic properties of doped semiconductors. vol 45. Berlin, Heidelberg: Springer Berlin Heidelberg, 1984

[81] Huang Y L, Chiu S P, Zhu Z X, et al. Variable-range-hopping conduction processes in oxygen deficient polycrystalline ZnO films. J Appl Phys, 2010, 107: 063715

[82] Paschoal W, Kumar S, Borschel C, et al. Hopping conduction in Mn ion-implanted GaAs nanowires. Nano Lett, 2012, 12: 4838

[83] Imran Z, Rafiq M A, Hasan M M. Charge carrier transport mechanisms in perovskite $CdTiO_3$ fibers. AIP Adv, 2014, 4: 067137

[84] Jian D, Lai J J, Lin Y F, et al. Electron hopping transport in 2D zinc oxide nanoflakes. 2D Mater, 2017, 4: 25028

[85] Yu D, Wang C, Wehrenberg B L et al. Variable range hopping conduction in semiconductor nanocrystal solids. Phys Rev Lett, 2004, 92: 216802

[86] Mukherjee J, Mannam R, Rao M S R. Variable range hopping crossover and magnetotransport in PLD grown Sb doped ZnO thin film. Semicond Sci Technolm, 2017, 32: 45008

[87] Li Z, Peng L, Zhang J, et al. Transition between Efros–Shklovskii and Mott variable-range hopping conduction in polycrystalline germanium thin films. Semicond Sci Technol, 2017, 32: 35010

[88] Paschoal W, Kumar S, Borschel C, et al. Hopping conduction in Mn ion-implanted GaAs nanowires. Nano Lett, 2012, 12: 4838

[89] Ma Y J, Zhang Z, Zhou F, et al. Hopping conduction in single ZnO nanowires. Nanotechnology, 2005, 16: 746

[90] Ali H, Khan U, Rafiq M A, et al. Richardson-Schottky transport mechanism in ZnS nanoparticles. AIP Adv, 2016, 6: 055306

[91] Gould R D, Bowler C J. DC electrical properties of evaporated thin films of CdTe. Thin Solid Films, 1988, 164: 281

[92] Altuntas H, Ozgit-Akgun C, Donmez I, et al. Current transport mechanisms in plasma-enhanced atomic layer deposited AlN thin films. J Appl Phys, 2015, 117: 155101

[93] Jeong D S, Park H B, Hwang C S. Reasons for obtaining an optical dielectric constant from the Poole-Frenkel conduction behavior of atomic-layer-deposited HfO_2 films. Appl Phys Lett, 2005, 86: 1

[94] Son S Y, Choi Y S, Kumar P, et al. Strain induced changes in gate leakage current and dielectric constant of nitrided Hf-silicate metal oxide semiconductor capacitors. Appl Phys Lett, 2008, 93: 153505

[95] Chiu F, Lee C, Pan T. Current conduction mechanisms in Pr_2O_3/oxynitride laminated gate dielectrics. J Appl Phys, 2009, 105: 74103

[96] Yeh C, Ma T P, Ramaswamy N, et al. Frenkel-Poole trap energy extraction of atomic layer deposited Al2O3 and HfxAlyO thin films. Appl Phys Lett, 2007, 91: 113521

[97] Weisse J M, Lee C H, Kim D R, et al. Fabrication of flexible and vertical silicon nanowire electronics. Nano Lett, 2012, 12: 3339

[98] Choueib M, Ayari A, Vincent P, et al. Evidence for Poole-Frenkel conduction in individual SiC nanowires by field emission transport measurements. J Appl Phys, 2011, 109: 1

[99] Ben-Chorin M, Möller F, Koch F. Nonlinear electrical transport in porous silicon. Phys Rev B, 1994, 49: 2981

[100] Lenz T, Richter M, Matt G J, et al. Charge transport in nanoparticular thin films of zinc oxide and aluminum-doped zinc oxide. J Mater Chem C, 2015, 3: 1468

[101] Hayat K, Rafiq M A, Rahman A, et al. Size-manipulation, compaction and electrical properties of barium manganite nanorods synthesized via the CHM method. Prog Nat Sci Mater Int, 2013, 23: 388

[102] Katzenmeyer A M, Léonard F, Talin A A, et al. Poole-frenkel effect and phonon-assisted tunneling in GaAs nanowires. Nano Lett, 2010, 10: 4935

[103] Cheung S K, Cheung N W. Extraction of Schottky diode parameters from forward current–voltage characteristics. Appl Phys Lett, 1986, 49: 85

[104] Rajan L, Periasamy C, Sahula V. Comprehensive study on electrical and hydrogen gas sensing characteristics of Pt/ZnO thin film based Schottky diodes grown on n-Si substrates by RF sputtering. IEEE Trans Nanotechnol, 2016, 15: 201

[105] Quereda J, Palacios J J, Agräit N, et al. Strain engineering of Schottky barriers in single- and few-layer MoS_2 vertical devices. 2D Mater, 2017, 4: 21006

[106] Ahmad M, Rasool K, Rafiq M A, et al. Effect of incorporation of zinc sulfide nanoparticles on carrier transport in silicon nanowires. Phys E, 2012, 45: 201

[107] Gokarna A, Pavaskar N R, Sathaye S D, et al. Electroluminescence from heterojunctions of nanocrystalline CdS and ZnS with porous silicon. J Appl Phys, 2002, 92: 2118

[108] Neville R C, Mead C A. Surface barriers on zinc oxide. J Appl Phys, 1970, 41: 3795

[109] Tsiarapas C, Girginoudi D, Georgoulas N. Electrical characteristics of Pd Schottky contacts on ZnO films. Mater Sci

Semicond Process, 2014, 17: 199

[110] Hussain I, Soomro M Y, Bano N, et al. Interface trap characterization and electrical properties of Au-ZnO nanorod Schottky diodes by conductance and capacitance methods. J Appl Phys, 2012, 112: 64506

[111] Sze M. Physics of semiconductor devices. Vol 10. Wiley-Interscience, 1995

[112] Toumi S, Ouennoughi Z, Strenger K C, et al. Determination of Fowler-Nordheim tunneling parameters in metal-oxide-semiconductor structure including oxide field correction using a vertical optimization method. Solid State Electron, 2016, 122: 56

[113] Chiou Y L, Gambino J P, Mohammad M. Determination of the Fowler-Nordheim tunneling parameters from the Fowler-Nordheim plot. Solid State Electron, 2001, 45: 1787

[114] Lenzlinger M, Snow E H. Fowler-nordheim tunneling into thermally grown SiO$_2$. J Appl Phys, 1969, 40: 278

[115] Fang X, Bando Y, Gautam U K, et al. Inorganic semiconductor nanostructures and their field-emission applications. J Mater Chem, 2008, 18: 509

[116] Zhao Q, Zhang H Z, Zhu Y W, et al. Morphological effects on the field emission of ZnO nanorod arrays. Appl Phys Lett, 2005, 86: 1

[117] She J, Xiao Z, Yang Y, et al. Correlation between resistance and field emission performance of individual ZnO one-dimensional nanostructures. ACS Nano, 2008, 2: 2015

[118] Sun L, Zhou X, Lin Z, et al. Effects of ZnO quantum dots decoration on the field emission behavior of graphene. ACS Appl Mater Interfaces, 2016, 8: 31856

[119] Zhou X, Lin T, Liu Y, et al. Structural, optical, and improved field-emission properties of tetrapod-shaped Sn-doped ZnO nanostructures synthesized via thermal evaporation. ACS Appl Mater Interfaces, 2013, 5: 10067

[120] Shen G, Bando Y, Ye C, et al. Synthesis, characterization and field-emission properties of bamboo-like β-SiC nanowires. Nanotechnology, 2006, 17: 3468

[121] Li L, Fang X, Chew H G, et al. Crystallinity-controlled germanium nanowire arrays: potential field emitters. Adv Funct Mater, 2008, 18: 1080

[122] Zhu Y W, Yu T, Cheong F C, et al. Large-scale synthesis and field emission properties of vertically oriented CuO nanowire films. Nanotechnology, 2005, 16: 88

[123] Young S J, Yang C C, Lai L T. Review—growth of Al-, Ga-, and In-Doped ZnO nanostructures via a low-temperature process and their application to field emission devices and ultraviolet photosensors. J Electrochem Soc, 2017, 164: B3013

[124] Chen L, Yu H, Zhong J, et al. Graphene field emitters: a review of fabrication, characterization and properties. Mater Sci Eng B, 2017, 220: 44

[125] Hsieh C T, Chen J M, Lin H H et al. Field emission from various CuO nanostructures. Appl Phys Lett, 2003, 83: 3383

[126] Pan H, Poh C K, Zhu Y, et al. Novel CdS nanostructures: synthesis and field emission. J Phys Chem C, 2008, 112: 11227

[127] Zhai T, Fang X, Bando Y, et al. Morphology-dependent stimulated emission and field emission of ordered CdS nanostructure arrays. ACS Nano, 2009, 3: 949

[128] Gautam U K, Fang X, Bando Y, et al. Synthesis, structure, and multiply enhanced field-emission properties of branched ZnS nanotube In nanowire core shell heterostructures. ACS Nano, 2008, 2: 1015

[129] Yun K N, Sun Y, Han J S, et al. High-performance field-emission properties of boron nitride nanotube field emitters. ACS Appl Mater Interfaces, 2017, 9: 1562

[130] Zener C. A theory of the electrical breakdown of solid dielectrics. Proc R Soc A Math Phys Eng Sci, 1934, 145: 523

[131] Ionescu A M, Riel H. Tunnel field-effect transistors as energy-efficient electronic switches. Nature, 2011, 479: 329

[132] Seabaugh A C, Zhang Q. Low-voltage tunnel transistors for beyond CMOS logic. Proc IEEE, 2010, 98: 2095

[133] Nikonov D E, Young I A. Overview of beyond-CMOS devices and a uniform methodology for their benchmarking. Proc IEEE, 2013, 101: 2498

[134] Avci U E, Hasan S, Nikonov D E, et al. Understanding the feasibility of scaled III–V TFET for logic by bridging atomistic simulations and experimental results. Symposium on VLSI Technology (IEEE), 2012: 183

[135] Moselund K E, Ghoneim H, Björk M T, et al. Comparison of VLS grown Si NW tunnel FETs with different gate stacks. Proceedings of the 39th European Solid-State Device Research Conference (IEEE), 2009: 448

[136] Hu C, Patel P, Bowonder A, et al. Prospect of tunneling green transistor for 0.1V CMOS. International Electron Devices Meeting, IEDM, 2010

[137] Mayer F, Le Royer C, Damlencourt J F, et al. Impact of SOI, Si$_{1-x}$Ge$_x$OI and GeOI substrates on CMOS compatible tunnel FET performance. International Electron Devices Meeting, 2008: 1

[138] Aydin C, Zaslavsky A, Luryi S, et al. Lateral interband tunneling transistor in silicon-on-insulator. Appl Phys Lett, 2004, 84: 1780

[139] Hansch W, Fink C, Schulze J et al. Vertical MOS-gated Esaki tunneling transistor in silicon. Thin Solid Films, 2000, 369: 387

[140] Koga J, Toriumi A. Negative differential conductance in three terminal silicon tunneling device. Appl Phys Lett, 1996, 69: 1435

[141] Reddick W M, Amaratunga G A J. Silicon surface tunnel transistor. Appl Phys Lett, 1995, 67: 494

[142] Baba T. Proposal for surface tunnel transistors. Jpn J Appl Phys, 1992, 31: L455

[143] Takeda E, Matsuoka H, Igura Y, et al. A band to band tunneling MOS device (B^{2}T-MOSFET)—a kind of "Si quantum device". Tech Dig Int Electron Devices Meet, 1988: 402

[144] Banerjee S, Richardson W, Coleman J, et al. A new three-terminal tunnel device. IEEE Electron Device Lett, 1987, 8: 347

[145] Quinn J J, Kawamoto G, McCombe B D. Subband spectroscopy by surface channel tunneling. Surf Sci, 1978, 73: 190

[146] Fiori G, Iannaccone G. Ultralow-voltage bilayer graphene tunnel FET. IEEE Electron Device Lett, 2009, 30: 1096

[147] Wu P, Prakash A, Appenzeller J. First demonstration of band-to-band tunneling in black phosphorus. Nat Commun, 2015, 6: 8948

[148] Lan Y W, Torres C M, Tsai S H, et al. Atomic-monolayer MoS$_2$ band-to-band tunneling field-effect transistor. Small, 2016, 12: 5676

[149] Roy T, Tosun M, Hettick M, et al. 2D–2D tunneling field-effect transistors using WSe$_2$/SnSe$_2$ heterostructures. Appl Phys Lett, 2016, 108: 83111

[150] Doan M H, Jin Y, Adhikari S, et al. Charge transport in MoS$_2$/WSe$_2$ van der Waals heterostructure with tunable inversion layer. ACS Nano, 2017, 11: 3832

[151] Roy T, Tosun M, Cao X, et al. Dual-gated MoS$_2$/WSe$_2$ van der Waals tunnel diodes and transistors. ACS Nano, 2015, 9: 2071

[152] Knoch J, Appenzeller J. A novel concept for field-effect transistors—the tunneling carbon nanotube FET. Device Research Conference, 2005: 153

[153] Appenzeller J, Lin Y M, Knoch J, et al. Band-to-band tunneling in carbon nanotube field-effect transistors. Phys Rev Lett, 2004, 93: 196805